Fluctuations of cell geometry and their nonequilibrium thermodynamics in living epithelial tissue

M. Olenik,[1,*] J. Turley,[1,2,*] S. Cross,[2] H. Weavers,[2] P. Martin,[2] I. V. Chenchiah,[1] and T. B. Liverpool[1]
[1]*School of Mathematics, University of Bristol - Bristol BS8 1UG, United Kingdom*
[2]*School of Biochemistry, University of Bristol - Bristol BS8 1TW, United Kingdom*

(Received 30 November 2021; accepted 18 November 2022; published 13 January 2023)

We measure different contributions to entropy production in a living functional epithelial tissue. We do this by extracting the functional dynamics of development while at the same time quantifying fluctuations. Using the translucent *Drosophila melanogaster* pupal epithelium as an ideal tissue for high-resolution live imaging, we measure the entropy associated with the stochastic geometry of cells in the epithelium. This is done using a detailed analysis of the dynamics of the shape and orientation of individual cells which enables separation of local and global aspects of the tissue behavior. Intriguingly, we find that we can observe irreversible dynamics in the cell geometries but without a change in the entropy associated with those degrees of freedom, showing that there is a flow of energy into those degrees of freedom. Hence, the living system is controlling how the entropy is being produced and partitioned into its different parts.

DOI: 10.1103/PhysRevE.107.014403

I. INTRODUCTION

A tissue is a group of similar cells that function together as a unit. Hence, there is a hope that ideas and techniques to describe many particle systems from condensed matter physics will be helpful to understand their function [1]. There have already been some significant successes following this line of reasoning. The mechanical influences on the dynamic interplay between cells in epithelial tissues have been shown to be important for a diverse array of biological processes from embryonic development and growth [2,3] to healing of wounds [4–7] and other pathologies like cancer [8]. Due to their importance in understanding tissues, there has been much work on quantifying and inferring these forces [9–12].

However, self-sustaining tissue is different from a collection of cells (its constituent parts) due to a variety of stochastic [13,14] feedback processes and information flow essential for life to function. More is different, but in not quite the same way as in traditional condensed matter [1]. To consider the physical constraints on biological function in the most realistic context, our focus here is quantifying *functional* living tissue [15] *in-vivo*. By doing this we aim to contrast with recent work on collective cell behavior in *in-vitro* sheets of cells [16–21] or *ex-vivo* tissue extracts [6]. We explore this difference by quantifying the fluctuations as well as the dynamics of various geometric quantities in living tissue at cellular scales, looking for signatures of functionality [22]. From analysis of the fluctuations we measure the system's entropy and how it evolves in time. The fact that entropy increases for irreversible adiabatic processes (the second law of thermodynamics) is one of the touchstones of modern physics. It is not clear if entropy is even a useful concept in living multicellular organisms, which of course are *not* adiabatic, nor at equilibrium. In addition, the question of how entropy evolves in living multicellular organisms remains an open question which we try to address here. A key part of our analysis involves defining a *partial* entropy [23], depending only on a subset of the total number of degrees of freedom (d.o.f.) available. The other degrees of freedom can then be viewed as a part of a reservoir in contact with these d.o.f.

We also precisely quantify a well-known analogy [24] to the breaking of rotational symmetry occurring in the transitions from an isotropic to an ordered mesophase in a liquid crystal [25] and the global shape and orientational order occurring in regions of developing tissue [26]. We map the shape and orientations of cells in the epithelium to a model liquid crystal. While easy to see for *in-vitro* sheets of confluent elongated cells like fibroblasts [16,17], it is harder to make this analogy for the more isotropic cells found in functional tissue. This also addresses the question of whether the cells show nematic [27] or polar (ferroelectric) [28] liquid crystalline order. We show unambiguously that epithelial cells in a living functional tissue show nematic order on large scales but polar order on very small scales, which quickly decays to zero over a correlation length comparable to the size of a single cell. Furthermore, the irreversible process [29,30] of epithelial growth is indicated by the amount of liquid crystal (nematic) order increasing with time while at the same time the associated observed *partial* (information) entropy [31,32] remains constant.

We study epithelial tissue at a well-characterized stage of development where the hinge region is contracting and stretching the wing blade. We are investigating this, focusing on the fluctuations on the cellular scale [15,33]. We show that throughout a 1-h period of observation, despite the increasing average orientational order, the probability distribution of cell shapes and orientations follows a universal form which remains steady, but that while the individual cells behavior fluctuates widely, their average behavior evolves in a precise, deterministic way according to an equation of motion

[*]These authors contributed equally to this work.

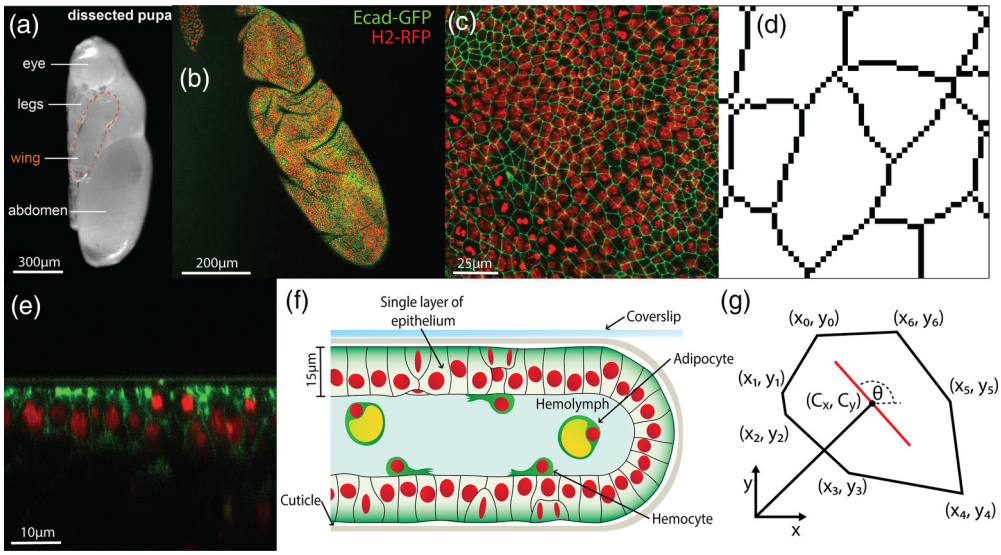

FIG. 1. (a) Translucent *Drosophila* pupa after dissection from its puparium [37,43]. (b) Low magnification of the entire transgenic pupal wing; the total wing length is 800 μm and the width is 250 μm. The green is E-cadherin–GFP, which labels the cell's adherens junctions, and the red is histone-RFP, which labels the cell nuclei. (c) Pupal wing tissue. (d) A high-magnification (binary) view of cell boundaries. (e) High-magnification cross section of the wing. (f) A schematic diagram of the cross section of the wing. (g) Geometric characterization of a cell and its boundary. Scale bars as indicated.

which we are able to obtain. This implies that the average dynamics are tightly coupled to the fluctuations and vice versa, providing a special type of steady state where the density of states remains constant even while the system is evolving continually in time [34]. This suggests that zero entropy production, in the presence of irreversible dynamics, can be a way to identify healthy functional living tissue. Using this entropy, we are able to separate the fluctuations [13,35] in the tissue at the cellular level from the large-scale changes occurring that lead to development, growth, and morphogenesis.

Drosophila is highly genetically tractable and is well characterized as a model of embryonic development and disease [36]. Here we study the pupal stage of its life cycle because pupae are translucent and immobile [see Fig. 1(a)]. More specifically, we investigate pupal wings [see Figs. 1(b) and 1(f)], which enable viewing of a flat two-dimensional (2D) surface of epithelial cells, to gather data-rich high-resolution *in-vivo* images with relative ease [37]. These images of the wing provide us with a unique opportunity for a level of analysis that is currently not possible in other systems due to their opacity and the difficulty in obtaining equivalent quality *in-vivo* data.

Confocal movies were captured from 18 h post pupal formation. The pupae were first dissected and removed from their puparium. This allowed us to directly view the wing [see Fig. 1(f)] and to gather confocal time-lapse movies of the living wing tissue, details of which are in the Supplemental Material [38] [37]. An example image from a movie is given in Fig. 1(c), with a cross-sectional view in Fig. 1(e). From the experimental data we generated binary images, as shown in Fig. 1(d) [39–42]. The cell boundaries were fitted to polygons (∼5–16 edges and where a single cell-cell boundary can have more than one edge) suitable for efficient mathematical analysis [see Fig. 1(g)].

Using these movies, we can perform a detailed statistical analysis of the evolution in time of the shapes, sizes, and orientations of cells, looking not only at their typical behavior but also their fluctuations. This will allow us to maximize the amount of useful information that we can extract from these observations. Hence, this will put us in the position to most accurately quantify what happens to such tissues after perturbations such as wounds.

II. METHODS

A. Experimental methods

Transgenic *Drosophila* were used that expressed the endogenous E-cadherin protein artificially tagged with green fluorescent protein (GFP). E-cadherin is a cell-cell adhesion molecule; this means the fluorescent protein is localized at the cell membranes, allowing easy identification of cell-cell boundaries via microscopy [see Fig. 1(c)]. Images were taken of pupae at 18 h after puparium formation (APF). To gain images of the pupae wings, first the pupae were dissected to remove the puparium case. This allowed us to directly view the wing [37]. The pupae were transferred to an imaging dish, with the wing in direct contact with the cover glass. Wings from transgenic *Drosophila* pupae labeled with E-cadherin–GFP and histone-RFP were imaged on a Leica SP8 confocal microscope. *Z* stacks were taken through the three-dimensional (3D) wing (with *Z* slices at 0.75-μm intervals) and images were taken every 5 min. This produced a time-lapse video of the healthy, developing tissue. Each image consists of a series of different heights through the tissue (*Z* stacks) [37]. The individual 3D stacks were transformed into 2D images using a modified version of the Stack Focuser plugin for FIJI [42]. The plugin works by selecting the most in-focus pixel for each (x, y). The most in-focus pixel is the

one with the highest variance of intensity in the surrounding pixels [42].

B. From experimental data to binary image

The experimental data, the focused 2D images, were processed on the Modular Image Analysis plugin for FIJI [39–42].

The images of the cell boundaries were enhanced using the WEKA pixel classification plugin, giving us a probability image [44]. Then, a median filter was applied to the image, which removed noise from the cell centres while retaining definition of the cell-cell boundaries. Finally, cell boundaries were obtained using the watershed transform. This converted the probability image into a binary one, with the boundaries labeled in black and cell in white [44]. A close-up of experimental data that has been processed into binary is in Fig. 1(d). To calculate the properties of each cell they must first be approximated with a polygon. These polygons will be used for analyses later.

C. From binary image to polygons

With these images, each cell was first identified and colored. Hence, the contours between cells were able to be determined and detected. Once the contours were identified, they were fitted with polygons. Thus, the boundaries of each cell were approximated by respective polygons.

Polygons that are clearly not cells can be selectively discounted from the image, e.g., these could be folds in the wing where the cells are out of the frame of reference in which image slices are taken. In the Supplemental Material [38] there is further information about how we identify and discount these polygons.

An example of a polygon is shown in Fig. 1(g). This polygon approximates a cell in one of the binary images. (C_x, C_y) is the centroid (center of mass) of the polygons. The vertices are labeled counterclockwise (this will be important in later calculations). Some notation for a polygon with n vertices in calculations $\boldsymbol{r}_n = \boldsymbol{r}_0$ [45].

D. Mathematical tools

We summarize here the theoretical tools we developed to quantify the shapes and orientations of individual cells. These local properties were used to find global averages and determine how they changed with time. The area of a polygon can be obtained from taking the double integral of the domain of the shape,

$$A = \iint_A dx\, dy. \tag{1}$$

E. Centroid

The center of the polygon (a measure of its location) is called its centroid. The centroid is the mean point of the polygon. This is where the moments of the shape are balanced. As the polygons are 2D shapes, the centroid will be a 2D vector. Each component was calculated by taking the double integral of the x or y over the domain of the polygon, then dividing by the area,

$$C_x = \frac{1}{A}\iint_A x\, dx\, dy, \tag{2}$$

$$C_y = \frac{1}{A}\iint_A y\, dx\, dy. \tag{3}$$

F. Shape tensor

The distribution of any molecule (e.g., a protein) in each cell (polygon) can be described by a second rank tensor defined by the second moment of the area weighted with the density of that molecule. Reminiscent of the inertia tensor, it is a measure of the variance of concentration of a molecule within a cell from its centroid in different directions. It therefore encodes information about the shape and orientation of each molecule distribution within the cell. It is defined as

$$\boldsymbol{s} = \begin{pmatrix} s_{xx} & s_{xy} \\ s_{xy} & s_{yy} \end{pmatrix}, \tag{4}$$

where

$$s_{xx} = -\frac{1}{A^2}\iint_A f(x', y')y'^2\, dx'\, dy', \tag{5}$$

$$s_{xy} = \frac{1}{A^2}\iint_A f(x', y')x'y'\, dx'\, dy', \tag{6}$$

$$s_{yy} = -\frac{1}{A^2}\iint_A f(x', y')x'^2\, dx'\, dy', \tag{7}$$

with $y' = y - C_y$, $x' = x - C_x$ and $f(x', y')$ the concentration of said molecule. Here we have averaged over all species in the cell and taken $f(x', y') = 1$. It is a dimensionless quantity. Details of its computation are given in the Supplemental Material [38,45].

G. Shape factor

From the shape tensor we can also construct a scalar, the shape factor which measures how elongated a shape is, with 0 being a round shape and approaching 1 is a very long thin shape. The shape factor is given by

$$s_f = \left|\frac{\lambda_2 - \lambda_1}{\lambda_2 + \lambda_1}\right|, \tag{8}$$

with $s_f \in (0, 1)$ as $\lambda_1, \lambda_2 > 0$, where λ_1 and λ_2 are eigenvalues of the shape tensor $\boldsymbol{s}$. Isotropic shapes are shapes with no clear major axis that would give it an orientation. For shapes that are isotropic, their eigenvalues are a similar length, making $|\lambda_1 - \lambda_2|$ small and hence giving a s_f close to 0, whereas elongated shapes will have a one large eigenvalue and one small, giving $|\lambda_1 - \lambda_2|$ a much larger value.

H. Orientation

We define the orientation as the direction of the long axis of the polygons, as shown in Fig. 1(g). The shape tensor cannot distinguish between the front or back of the polygon, so the orientation is only defined modulo π. The orientation is defined by the eigenvalues $\lambda_2 > \lambda_1 > 0$ and eigenvectors $\boldsymbol{v}_1, \boldsymbol{v}_2$ of $\boldsymbol{s}$. The eigenvector corresponding to the smallest

eigenvalue of $\boldsymbol{s}$ determines the major (long) axis and hence the orientation. If $\boldsymbol{v}_1$ is the eigenvector of the smallest eigenvalue, and ϑ is the angle of orientation taken from the x axis, then

$$\vartheta = \arctan\left(\frac{v_{12}}{v_{11}}\right) \quad \text{where} \quad \boldsymbol{v}_1 = (v_{11}, v_{12}), \tag{9}$$

$$\theta = \vartheta[\pi]. \tag{10}$$

It is more convenient for us to work with a q tensor, which is a traceless symmetric tensor created by $\boldsymbol{q} = \boldsymbol{s} - \mathrm{Tr}(\boldsymbol{s})\boldsymbol{I}$, where $\boldsymbol{I}$ is the identity matrix. $\boldsymbol{q} = \begin{pmatrix} q_1 & q_2 \\ q_2 & -q_1 \end{pmatrix} \neq 0$ implies an oriented tissue, and the more oriented a tissue, the greater the value of $\|\boldsymbol{q}\|^2 = \frac{\sqrt{2}}{2}\mathrm{Tr}(\boldsymbol{q}^2)$. Now we can take the mean and standard deviation of $\hat{\boldsymbol{q}}_i$ for each image,

$$Q\hat{\boldsymbol{Q}} = \frac{1}{N}\sum_{i=1}^{N}\hat{\boldsymbol{q}}_i, \tag{11}$$

$$\sigma_q^2 = \frac{1}{N}\sum_{i=1}^{N}\|\hat{\boldsymbol{q}}_i - \hat{\boldsymbol{Q}}\|^2 \quad , \tag{12}$$

where $\|\|$ is the Frobenius norm.

I. Polarization

Calculating a cell's polarization requires the use of a third rank tensor. To simplify calculations, we first translate and rotate the shape, $\mathbf{r} \to \mathbf{r}' = \mathbf{R}(\theta)^{-1} \cdot (\mathbf{r} + \mathbf{t})$, such that its centroid is at the origin with its major (long) axis oriented along the y' axis and the minor axis along the x' axis. The components of the polarization in the x' and the y' direction are given by T'_{xxx} and T'_{yyy}, respectively defined below. The polarization vector is then defined as $\boldsymbol{p}'(\mathbf{r}') = \frac{1}{A^{5/2}}(T'_{xxx}, T'_{yyy})$, where

$$T'_{xxx} = \iint_A x'^3\, dx'\, dy', \tag{13}$$

$$T'_{yyy} = \iint_A y'^3\, dx'\, dy'. \tag{14}$$

Once the polarization vector has been calculated, the reverse rotation, $\boldsymbol{p}(\mathbf{r}) = \mathbf{R}(\theta) \cdot \boldsymbol{p}'(\mathbf{r}')$, gives its value in the original coordinates. Similarly to the orientation, we can take the mean and standard deviation of $\hat{\boldsymbol{p}}_i$ for each image:

$$P\hat{\boldsymbol{P}} = \frac{1}{N}\sum_{i=1}^{N}\hat{\boldsymbol{p}}_i, \tag{15}$$

$$\sigma_p^2 = \frac{1}{N}\sum_{i=1}^{N}(\hat{\boldsymbol{p}}_i - \hat{\boldsymbol{P}})^2. \tag{16}$$

J. Theoretical model

Given cells whose shape is given by the tensor $\boldsymbol{q}$, we study the noisy growth of macroscopic orientation of the tissue along an arbitrary axis making an angle ϕ to the x axis. We start with a function $H(\boldsymbol{q}, q_0) = \sum_{i,j=1}^{2}\frac{1}{2}\delta q_i A_{ij}\delta q_j + O(\|\delta\boldsymbol{q}\|^3)$, where $\delta\boldsymbol{q} = \boldsymbol{q} - q_0\boldsymbol{n}$, which is minimized when the cell is oriented along an axis given by the tensor $\boldsymbol{n} = \begin{pmatrix} \cos 2\phi & \sin 2\phi \\ \sin 2\phi & -\cos 2\phi \end{pmatrix} = \begin{pmatrix} n_1 & n_2 \\ n_2 & -n_1 \end{pmatrix}$. The most general form of the 2×2 matrix A_{ij} which is rotationally invariant is given by $A_{ij} = A_0\delta_{ij} + A_1 n_i n_j$, with δ_{ij} being the Kronecker delta function and A_0, A_1 functions of the tension in the tissue . The dynamics, which is a combination of gradient flow towards the minimum of H and nonequilibrium stochastic driving, is described by Langevin equations (stochastic differential equations) for the tensor $\boldsymbol{q}$ and parameter q_0,

$$\frac{dq_i}{dt} = -\frac{\partial H}{\partial q_i} + \xi_i(t) = -A_{ij}(q_j - q_0 n_j) + \xi_i \tag{17}$$

$$\frac{dq_0}{dt} = k_0 - \frac{\partial H}{\partial q_0} + \xi_0(t), \quad k_0 > 0 \quad . \tag{18}$$

We emphasize that this means that the dynamics of individual cells are highly stochastic and fluctuate strongly in time. The fact that $k_0 > 0$ implies that shape orientational order is increasing. $q_0(t)$, $\boldsymbol{q}(t)$ have fluctuations that are encoded in the white noises

$$\langle\xi_i\rangle = 0, \quad \langle\xi_i(t)\xi_j(t')\rangle = 2D_i\delta_{ij}\delta(t - t'), \tag{19}$$

where $i, j \in \{0, 1, 2\}$ and the constant parameters k_0, A_0, A_1 control the behavior. We take $D_1 = D_2 = D$ and $\delta(t - t')$ is Dirac delta function . A key part of our analysis will be determining what parameters of the model are consistent with the data.

Defining $\vec{X} = (q_0, q_1, q_2)$, the Langevin equations for the fluctuating variables are equivalent to a Fokker-Planck equation for the probability density $P(\vec{X})$:

$$\partial_t P + \sum_{i=1}^{3}\nabla_i(V_i P) = 0, \quad V_i = (v_i - \nabla_i H - D_i\nabla_i \ln P), \tag{20}$$

where $\nabla_i = \partial/\partial X_i$. The set of equations above have a steady-state probability density given by

$$P_{ss}(\boldsymbol{q}, A) = \frac{1}{Z}e^{-h(\boldsymbol{q},A)}; \quad h = H/D_0 \tag{21}$$

and dynamical system

$$\frac{d\bar{\boldsymbol{q}}}{dt} = -\left(1 - \frac{D}{D_0}\right)\boldsymbol{A} \cdot (\bar{\boldsymbol{q}} - \overline{q_0}\boldsymbol{n}) \tag{22}$$

$$\frac{d\overline{q_0}}{dt} = k_0, \tag{23}$$

as long as $D_0 > D$. It is important to note that $\min(h) = 0$ is bounded below [34].

Starting with an initial typical value at $t = 0$ of $\overline{q(0)} = \theta_0$, $\overline{\boldsymbol{q}(0)} = \theta_0\boldsymbol{n}$, we find $q_0(t) = \theta_0 + k_0 t$, $\overline{\boldsymbol{q}(t)} = q_0(t)\boldsymbol{n}$. This allows us to study statistically the behavior of different trajectories (experimental samples). First, coordinate axes are rotated so the orientation axis is along the x axis. With this we can express the steady-state probability density in terms of the deviations from the typical values.

Hence, we set $\boldsymbol{q}(t) = \overline{\boldsymbol{q}(t)} + \delta\boldsymbol{q}(t)$, $q_0 = \overline{q_0(t)} + \delta q_0(t)$, to obtain

$$P_{ss}(\delta\boldsymbol{q}, \delta q_0) = \frac{1}{Z'}\exp\left[-\frac{1}{D_0}F(\delta q_1, \delta q_2, \delta q_0)\right], \tag{24}$$

where

$$F = \frac{(A_0 + A_1)}{2}(\delta q_1)^2 + \frac{A_0}{2}(\delta q_2)^2 \tag{25}$$

and Z' is chosen so that $\int d\boldsymbol{q}dq_0 P_{ss} = 1$.

From this we obtain

$$\langle(\delta q_1)^2\rangle = \frac{D_0}{A_0 + A_1},$$
$$\langle(\delta q_2)^2\rangle = \frac{D_0}{A_0}.$$

From this it follows that

$$\langle\|\boldsymbol{q}\|\rangle = q_0(t) = \theta_0 + k_0 t. \tag{26}$$

From the data it thus follows that we can extract C, k_B, a_0, b_0, θ.

III. RESULTS

A. Analysis

In this stage in development of the wing tissue, the cells are reducing their area at a linear rate. At the same time the number of cells is also increasing linearly.

B. Shape tensor

Each cell (polygon) can be described by a second rank tensor, which we call the shape tensor ($\boldsymbol{S}$), a measure of the variance of the shape of a polygon from its centroid in different directions. Encoding information about the shape and orientation of each cell, it is similar to the texture tensors introduced in Refs. [46,47]. To compare cells of different sizes, it is made dimensionless by dividing by the area squared (see Supplemental Material [38]).

C. Cell shape factor

We can gain information about a cell's shape from the difference between the eigenvalues of the shape tensors, which we call the shape factor. The shape factor lies between [0, 1). When eigenvalues are similar, this gives a low shape factor (close to 0), indicating an isotropic, nonoriented shape. A high shape factor implies an elongated shape with vastly different eigenvalues. For more details about shape tensors/factors see the Supplemental Material [38].

Figures 2(a) and 2(b) show the shape factor heat map and histogram, respectively, for a typical image. Figure 2(c) shows how the average shape factor evolves with time. There is a clear linear increase with time. This means cells are becoming increasingly elongated as the tissue develops. The cause of the elongation is the concentration of cells in the hinge, which applies tension across the blade where we are imaging [15].

D. Cell orientation

We define the cell orientation as the angle $\theta \in [0, \pi)$ between the major axis of the cell and the x axis [see Fig. 1(g)]. The orientation (major) axis is the eigenvector of the shape tensor with the smallest eigenvalue. The orientation axis, invariant under reflection, is $\pi-$periodic, $\theta = \theta + \pi$. Figure 2(d) shows a heat map of the orientations from the same image as Fig. 2(a). It is clear from the heat map that there is a global orientation of this tissue. The most common cell color, yellow-green, indicates a mean orientation of $\sim\pi/6$.

The mean orientation, determined by orientation of the pupa wing on the slide, is arbitrary. However, the standard deviation of cell orientations around the mean remains consistent between samples at the same developmental stage and indicates how oriented the tissue is; the smaller the standard deviation, the more oriented it is. Figure 2(f) shows that the standard deviation is a linearly decreasing function of time, implying that an increasing number of cells are oriented in the same direction as time increases.

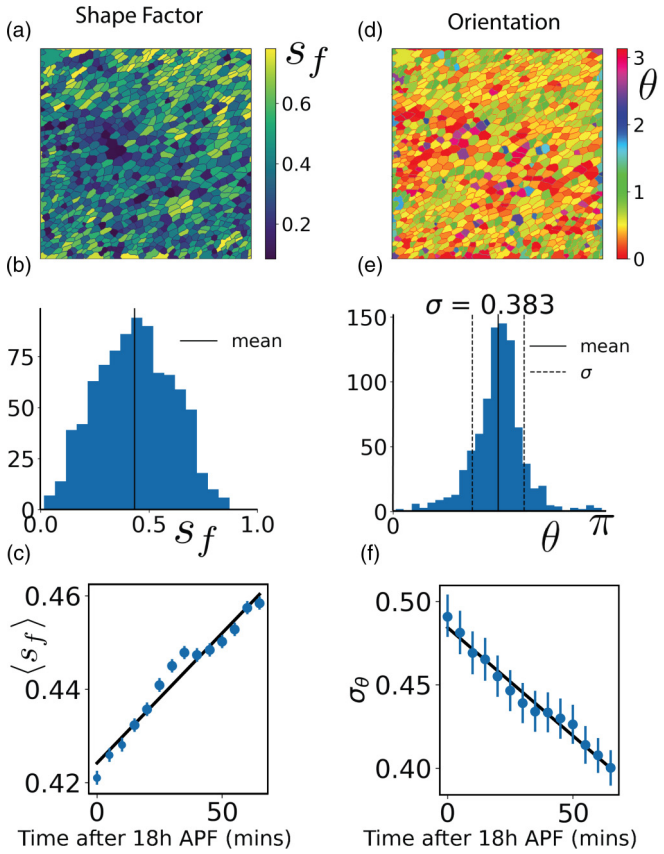

FIG. 2. (a) The shape factor of cells; elongated and thin shapes have high values (yellow), isotropic (nonoriented) shapes have low values (blue). (b) The distribution of the shape factor. The black line shows the mean. (c) The mean shape factor increases linearly with time. (d) Heat map showing the orientation of each cell relative to the x axis of a single sample. (e) The distribution of orientations in the sample in part (c) but rotated such that the mean is at $\frac{\pi}{2}$. The black line shows the mean. The standard deviation is in the subtitle. (f) The standard deviation of the orientation averaged over 15 samples decreases linearly with time. (Error bars are root mean square errors.)

We can more precisely quantify the fluctuating growth of the tissue by studying the evolution of the whole shape tensor. We define a q tensor, a traceless symmetric tensor created by $\boldsymbol{q} = \boldsymbol{S} - \mathrm{Tr}(\boldsymbol{S})\boldsymbol{I}$, where $\boldsymbol{I}$ is the identity matrix: $\boldsymbol{q} = \begin{pmatrix} q_1 & q_2 \\ q_2 & -q_1 \end{pmatrix} = \frac{q_0}{\sqrt{2}}\begin{pmatrix} \cos 2\theta & \sin 2\theta \\ \sin 2\theta & -\cos 2\theta \end{pmatrix} = q_0\hat{\boldsymbol{q}}$. If the norm, $\|\boldsymbol{q}\| \neq 0 \Rightarrow$ an elongated shape, and the more oriented a shape, the greater the norm $[\|\boldsymbol{q}\|^2 = \frac{1}{2}\mathrm{Tr}(\boldsymbol{q}^2) = q_0^2$, $\hat{\boldsymbol{q}}$ has unit norm and θ is orientation].

To determine the orientation of the tissue we calculate the average of the cell's q tensors, $\boldsymbol{Q} = \langle \boldsymbol{q} \rangle$. We define Q, its magnitude (norm), and write $\boldsymbol{Q} = Q\hat{\boldsymbol{Q}}$, where $\hat{\boldsymbol{Q}}$ is a unit tensor. We analyze the distribution of tensors using the standard deviation (σ_q). If $\frac{Q}{\sigma_q} \sim 1$, then the system is functionally oriented,

and if $\frac{Q}{\sigma_q} \ll 1$, it is functionally isotropic. We find typical values of $\frac{Q}{\sigma_q} \simeq 0.84$, indicating an oriented tissue. Details about the mean and standard deviation are in the Supplemental Material [38].

E. Cell polarization

The shape tensor is unable to identify whether a cell has any shape anisotropy along its main axes, which requires a third rank tensor. From this tensor we can define a polarization vector $\boldsymbol{p}$ (see Supplemental Material [38]). The polarization of a cell measures the skewness of its shape. The polarization of each cell $\boldsymbol{p}$ can be decomposed into magnitude and direction: $\boldsymbol{p} = p\hat{\boldsymbol{p}}$, where $p = |\boldsymbol{p}|$ and $\hat{\boldsymbol{p}} = (\cos\phi, \sin\phi)$. When this magnitude is large, the shape is highly polarized, and when the magnitude is small, the shape is not polarized. As above, to get an indication of whether the tissue has a global polarization, it is instructive to compute the average of the polarization vectors $\boldsymbol{P} = \langle \boldsymbol{p} \rangle = P\hat{\boldsymbol{P}}$ and standard deviation (σ_p). P is the magnitude of this average vector (how strong it is), and the unit vector $\hat{\boldsymbol{P}}$ indicates in which direction the tissue is polarized. If $\frac{P}{\sigma_p} \sim 1$, then the system is functionally polarized, and if $\frac{P}{\sigma_p} \ll 1$, it is functionally isotropic. Typically, values of $\frac{P}{\sigma_p} \simeq 0.021$, indicating isotropy with no polarization.

F. Correlations of the orientation and polarization

We also consider the orientation and polarization correlations of cells separated by distance R,

$$C_p(R) = \frac{1}{N_R} \sum_{R<|\boldsymbol{r}_i - \boldsymbol{r}_j|<R+dR} \langle \hat{\boldsymbol{p}}_i, \hat{\boldsymbol{p}}_j \rangle, \tag{27}$$

$$C_q(R) = \frac{1}{N_R} \sum_{R<|\boldsymbol{r}_i - \boldsymbol{r}_j|<R+dR} \langle \hat{\boldsymbol{q}}_i, \hat{\boldsymbol{q}}_j \rangle. \tag{28}$$

For the $\hat{\boldsymbol{q}}$ we use the Frobenius inner product. The functions C_p, C_q are plotted in Fig. 3(b). C_p has a small anticorrelation at small distances, after which the correlation function decays quickly to zero. It is negative at short distances, which implies that if a cell is polarized in one direction, its direct neighbors are likely to be polarized in the opposite direction, but that cells further than one cell apart are essentially uncorrelated. Therefore, while individual cells can be polarized, the tissue is not polarized at all. The fact that C_q does not decay to zero for large distances demonstrates that there is strong orientational order throughout the tissue. Hence, the tissue is oriented but not polarized.

G. Partial entropy production

We also analyze the distribution of cell shapes and orientations and its evolution in time and hence extract the flow of information (partial entropy) associated with it. At this point it is probably helpful to review some basic notions of thermodynamics and nonequilibrium statistical mechanics. We consider in general a macroscopic system plus its environment at fixed temperature, which together form an isolated composite. From the second law, the total entropy production is given by the sum of that produced by the system

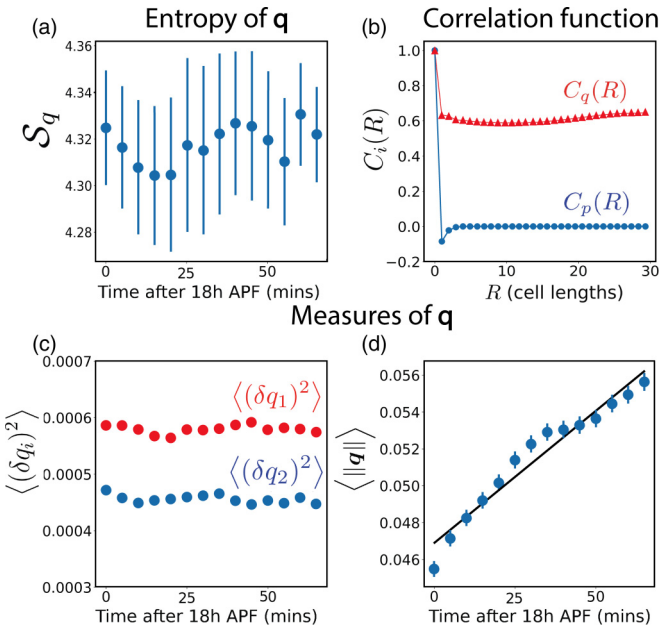

FIG. 3. (a) The entropy of the $\boldsymbol{q}$ tenser. Each point is the mean entropy of the videos. (b)The figure shows the correlation function of the polarization and the orientation, respectively. Distance by a typical cell length scale is defined by the square root of the mean area of the cells in each image. $C_p(R)$ at 1 cell length starts negatively and then decays exponentially to 0. $C_q(R)$ is correlated around 0.6 throughout the tissue (error bars are smaller than markers). c) $\langle(\delta q_1)^2\rangle$ and $\langle(\delta q_2)^2\rangle$ over the frames of the video (error bars are smaller than markers). (d) $\langle\|\boldsymbol{q}\|\rangle$ over the frames of the video. This increased linearly over time, and line of best fit is shown in black. (Error bars are root mean square errors.)

(sys) and its environment (env), $\dot{\mathcal{S}}_{\text{tot}} = \dot{\mathcal{S}}_{\text{sys}} + \dot{\mathcal{S}}_{\text{env}} \geqslant 0$, with $\dot{\mathcal{S}}_{\text{sys}} = \dot{\mathcal{S}}_{\text{env}} = 0$ at equilibrium. Typically when studying passive systems, we consider situations where the system does not perturb the environment, which can be considered to be at equilibrium, $\dot{\mathcal{S}}_{\text{env}} = 0$. For a passive system coupled to such a reservoir, starting in a nonequilibrium initial state and evolving towards a (possibly more-ordered) equilibrium state, we would then expect that $\dot{\mathcal{S}}_{\text{sys}} > 0$. We explore here what happens in a living functional tissue whose cells are becoming more orientationally ordered, in which the system corresponds to the degrees of freedom associated with the cell shape and orientations and the environment is everything else.

Defining the probability $\rho_{\boldsymbol{q}}$ of finding a cell with shape $\boldsymbol{q}$, we can calculate the *shape entropy*, the contribution to the entropy from shape fluctuations, $\mathcal{S}_{\boldsymbol{q}}(t) = -\sum_{\boldsymbol{q}} \rho_{\boldsymbol{q}} \ln \rho_{\boldsymbol{q}}$, and its evolution with time. A constant value for $\mathcal{S}_{\boldsymbol{q}}$ is consistent with our measurements to within the error bars [see Fig. 3(a)]. Hence, we find that the partial entropy production is on average zero, i.e., the entropy remains constant over the whole period of observation despite the increase in orientational order. The observation of irreversible dynamics of some observables *without* an increase in entropy associated with them is an indication of a flux of energy from the degrees of freedom under observation into other degrees of freedom (i.e., it implies that the environment or reservoir is itself not at equilibrium) [48,49]. We emphasize that this implies that

while $\dot{\mathcal{S}}_{\rm sys} = 0$, $\dot{\mathcal{S}}_{\rm env} > 0$ and the second law is still satisfied. To be concrete, the second law requires that $T\dot{\mathcal{S}}_{\rm sys} \geqslant \dot{E}$, where $\dot{E}$ is the rate of energy (heat) flow to the system from the environment and T is the temperature of the system (and reservoir). Since this active system has $\dot{E} \neq 0$, the fact that $\dot{\mathcal{S}}_{\rm sys} = 0$ implies that $\dot{E} < 0$ and there is a (steady) flow of energy (heat) to the environment from the system. Conversely, the second law also implies that $T\dot{\mathcal{S}}_{\rm env} \geqslant -\dot{E} > 0$.

Constant entropy for a subset of the degrees of freedom, however, is ideal for accurate information processing and quick response to external perturbations of those observables. This is because the accuracy threshold for any error-correction mechanism will not be changing [50–52].

H. Theory

We now develop a model of the development of tissue orientation along an axis with angle ϕ that can be compared quantitatively to what we observe in the experimental data. The aim is to describe the dynamics of the probability distribution of cell shapes encoded in the tensor $\boldsymbol{q} = \left(\begin{smallmatrix} q_1 & q_2 \\ q_2 & -q_1 \end{smallmatrix}\right)$. All the data is consistent with a steady-state probability density given by

$$P_{ss}(\boldsymbol{q}, q_0) = \frac{1}{Z} e^{-h(\boldsymbol{q}, q_0)}; \quad h = H/D_0, \tag{29}$$

where $H(\boldsymbol{q}, q_0) = \sum_{i,j=1}^{2} \frac{1}{2} \delta q_i A_{ij} \delta q_j + O(\|\delta \boldsymbol{q}\|^3)$, where $\delta \boldsymbol{q} = \boldsymbol{q} - q_0 \boldsymbol{n}$ with the orientation $\boldsymbol{n} = \left(\begin{smallmatrix} \cos 2\phi & \sin 2\phi \\ \sin 2\phi & -\cos 2\phi \end{smallmatrix}\right) = \left(\begin{smallmatrix} n_1 & n_2 \\ n_2 & -n_1 \end{smallmatrix}\right)$. Note that $\min(h) > -\infty$ must be bounded for Eq. (29) to make sense. The most general form of the matrix $\boldsymbol{A}$ which is rotationally invariant is given by $A_{ij} = A_0 \delta_{ij} + A_1 n_i n_j$. The *fluctuating* variables $q_0(t), q_1(t), q_2(t)$ capture the changes in cell shape which evolve *on average* according to the deterministic dynamical system

$$\frac{d\bar{\boldsymbol{q}}}{dt} = \boldsymbol{V}(\bar{\boldsymbol{q}}, \overline{q_0}) = -\boldsymbol{A} \cdot (\bar{\boldsymbol{q}} - \overline{q_0}\boldsymbol{n}) \tag{30}$$

$$\frac{d\overline{q_0}}{dt} = V_0(\bar{\boldsymbol{q}}, \overline{q_0}) = k_0. \tag{31}$$

It is helpful at this point to compare this with the stochastic dynamics of an equilibrium system with the same number of degrees of freedom $\boldsymbol{e}(t) = (e_0, e_1, e_2)$ and a Hamiltonian $\mathcal{H}(\boldsymbol{e})$ so that

$$\frac{de_i}{dt} = -\frac{\partial \mathcal{H}}{\partial e_i} + \xi_i(t), \tag{32}$$

$$\langle \xi_i \rangle = 0, \quad \langle \xi_i(t) \xi_j(t') \rangle = 2T \delta_{ij} \delta(t - t'). \tag{33}$$

This system has a steady state with density of states, $P_{\rm eq}(\boldsymbol{e}) = e^{-\mathcal{H}/T}$, with average constant values $\overline{e_i}$, which means in the steady state the average $\overline{\boldsymbol{e}(t)}$ evolves according to

$$\frac{d\overline{e_i}}{dt} = 0, \tag{34}$$

i.e., the d.o.f. do not change with time. The dynamical system of the average behavior is a trivial one: all velocities are on average zero and each realization of the system (or equivalently each experiment) simply fluctuates around the mean constant value. This is equivalent to a detailed balance condition that is required by all systems at equilibrium. Here, the existence of a nontrivial dynamical system [i.e., the fact that the right hand side (rhs) of Eqs. (30) and (31) are not zero] means that the living epithelium cannot be mapped to an equilibrium system. Consequently, detailed balance is also broken: there are nonzero currents $\vec{J}_{ss}(\boldsymbol{q}, q_0) = [\boldsymbol{V}(\boldsymbol{q}, q_0), V_0(\boldsymbol{q}, q_0)] P_{ss}(\boldsymbol{q}, q_0)$ which break detailed balance. Each realization (experiment) will fluctuate around these deterministic trajectories. Guided by the data, we will obtain values for A_0, A_1, k_0. This allows us to study statistically the behavior of different trajectories (experimental samples). First, coordinate axes are rotated so the orientation axis is along the x axis (i.e., $n_1 = 1, n_2 = 0$). With this we can express the steady-state probability density in terms of the deviations from the typical values $\overline{q_0(t)}, \overline{q_1(t)}, \overline{q_2(t)}$. From the data we can compute $\langle \|\boldsymbol{q}\| \rangle$, $\langle (\delta q_1)^2 \rangle$, and $\langle (\delta q_2)^2 \rangle$, as shown in Figs. 3(c) and 3(d), from which we can extract k_0, A_0, A_1 (see Supplemental Material [38]), though it is not clear how these relate to mechanical properties of the developing tissue.

IV. SUMMARY AND DISCUSSION

The ability to visualize the dynamic evolution of the spatial distribution of specific proteins within individual cells in tissue provided by high-resolution imaging holds promise for us eventually being able to extract the organizing principles behind tissue function and repair. This biological function happens in the presence of large fluctuations, both chemical and mechanical, hence these principles, whatever they turn out to be, must be robust to noise. It is the implications of this robustness that we focus on in this paper. Here we have tracked the concentration of junction proteins to quantify the dynamics of cell shapes, orientations, and polarization, measuring not only their averages but, most importantly, their fluctuations. In this context, the degrees of freedom associated with the shapes, orientations, and polarizations of the cells are the *system*, while everything else in the tissue we consider as the *environment*.

The experimental data in total paint a consistent picture. We observe irreversible dynamics of the cells becoming more elongated and the tissue becoming more oriented along a particular direction **n** without any associated change in entropy. We emphasize that this implies that while the rate of entropy production of the environment is nonzero, $\dot{\mathcal{S}}_{\rm env} > 0$, the rate of change of entropy associated with those degrees of freedom in the tissue $\dot{\mathcal{S}}_{\rm sys} = 0$. This implies a steady flow of energy from the reservoir to the system. Given that the reservoir is much larger than the system, $\mathcal{S}_{\rm sys} \ll \mathcal{S}_{\rm env}$, we note that it is also possible that at different points in development, the rate of change of entropy in the tissue $\dot{\mathcal{S}}_{\rm sys}$ can be nonzero, even negative.

We also find no macroscopic shape polarization of the tissue; i.e., we find nematic symmetry of the director axis, i.e., **n** and $-$**n** are equivalent. This can be explained by a model of cell shape and orientation that can be mapped to a nonequilibrium driven nematic liquid crystal. We find that while oriented, the tissues have no global polarization, and that cells that are polarized only affect other cells in their very close proximity. An observation from our data is that all these features are developed in the presence of strong local variation and fluctuations about the average behavior. This indicates a large but constant information entropy. Clearly this approach

can be extended to any group of observables in living tissue or other functional biological matter. This suggests an intriguing possibility that should be investigated further by studying the statistical dynamics of other chemical and geometrical quantities in tissue to see if zero rate of change of entropy with irreversible dynamics is a signature of functionality and homeostasis in healthy living organisms. This characterization of an unperturbed but dynamic, developing tissue will lay the groundwork for understanding what happens when these tissues are perturbed, for example, by cancer or wounding.

ACKNOWLEDGMENTS

The computational resources of the University of Bristol Advanced Computing Research Centre and the BrisSynBio HPC facility are gratefully acknowledged. M.O. acknowledges the support of the Wellcome Trust. J.T. acknowledges a MRC GW4 studentship. T.B.L. acknowledges support of Leverhulme Trust Research Project Grant No. RPG-2016-147 and BrisSynBio, a BBSRC/EPSRC Synthetic Biology Research Center (BBSRC Grant No. BB/L01386X/1).

[1] P. W. Anderson, Science **177**, 393 (1972).
[2] T. Lecuit and P. F. Lenne, Nat. Rev. Mol. Cell Biol. **8**, 633 (2007).
[3] L. Le Goff and T. Lecuit, Science **331**, 1141 (2011).
[4] P. Martin and J. Lewis, Nature (London) **360**, 179 (1992).
[5] W. Razzell, W. Wood, and P. Martin, Development **141**, 1814 (2014).
[6] R. J. Tetley, M. F. Staddon, D. Heller, A. Hoppe, S. Banerjee, and Y. Mao, Nat. Phys. **15**, 1195 (2019).
[7] J. Turley, I. V. Chenchiah, T. B. Liverpool, H. Weavers, and P. Martin, iScience, **25** 104778 (2022).
[8] B. Piersma, M. Hayward, and V. M. Weaver, Biochim. Biophys. Acta, Rev. Cancer **1873**, 188356 (2020).
[9] M. S. Hutson, Y. Tokutake, M.-S. Chang, J. W. Bloor, S. Venakides, D. P. Kiehart, Science **300**, 145 (2003).
[10] S. Ishihara and K. Sugimura, J. Theor. Biol. **313**, 201 (2012).
[11] K. Sugimura and S. Ishihara, Development **140**, 4091 (2013).
[12] R. Etournay, M. Popović, M. Merkel, A. Nandi, C. Blasse, B. Aigouy, H. Brandl, G. Myers, G. Salbreux, F. Jülicher *et al.*, Elife **4**, e07090 (2015).
[13] M. B. Elowitz, A. J. Levine, E. D. Siggia, and P. S. Swain, Science **297**, 1183 (2002).
[14] J. R. Chubb and T. B. Liverpool, Curr. Opin. Genet. Dev. **20**, 478 (2010).
[15] B. Aigouy, R. Farhadifar, D. B. Staple, A. Sagner, J.-C. Röper, F. Jülicher, and S. Eaton, Cell **142**, 773 (2010).
[16] G. Duclos, S. Garcia, H. G. Yevick, and P. Silberzan, Soft Matter **10**, 2346 (2014).
[17] G. Duclos, C. Erlenkämper, J.-F. Joanny, and P. Silberzan, Nat. Phys. **13**, 58 (2017).
[18] X. Li, R. Balagam, T.-F. He, P. P. Lee, O. A. Igoshin, and H. Levine, Proc. Natl. Acad. Sci. **114**, 8974 (2017).
[19] T. B. Saw, A. Doostmohammadi, V. Nier, L. Kocgozlu, S. Thampi, Y. Toyama, P. Marcq, C. T. Lim, J. M. Yeomans, and B. Ladoux, Nature (London) **544**, 212 (2017).
[20] K. Kawaguchi, R. Kageyama, and M. Sano, Nature (London) **545**, 327 (2017).
[21] D. Martella, L. Pattelli, C. Matassini, F. Ridi, M. Bonini, P. Paoli, P. Baglioni, D. S. Wiersma, and C. Parmeggiani, Adv. Healthcare Mater. **8**, 1801489 (2019).
[22] S. Brenner, Nature (London) **482**, 461 (2012).
[23] H. Ahmadzade, R. Gao, M. H. Dehghan, and Y. Sheng, J. Intell. Fuzzy Syst. **33**, 105 (2017).
[24] Y. Bouligand, Comptes Rendus Chim. **11**, 281 (2008).
[25] P. G. D. Gennes and J. Prost, *The Physics of Liquid Crystals* (Clarendon Press, Oxford, 1993).
[26] M. Duvert, Y. Bouligand, and C. Salat, Tissue and Cell **16**, 469 (1984).
[27] P. D. Olmsted and P. M. Goldbart, Phys. Rev. A **41**, 4578 (1990).
[28] X. Chen, E. Korblova, D. Dong, X. Wei, R. Shao, L. Radzihovsky, M. A. Glaser, J. E. MacLennan, D. Bedrov D. M. Walba *et al.*, Proc. Natl. Acad. Sci. USA **117**, 14021 (2020).
[29] L. Onsager, Phys. Rev. **38**, 2265 (1931).
[30] X. Fang, K. Kruse, T. Lu, and J. Wang, Rev. Mod. Phys. **91**, 045004 (2019).
[31] M. Plischke and B. Bergersen, *Equilibrium Statistical Physics* (World Scientific, 2005).
[32] W. Bialek, A. Cavagna, I. Giardina, T. Mora, E. Silvestri, M. Viale, and A. M. Walczak, Proc. Natl. Acad. Sci. **109**, 4786 (2012).
[33] T. Athilingam, P. Tiwari, Y. Toyama, and T. E. Saunders, in *Seminars in Cell & Developmental Biology*, Vol. 120 (Elsevier, New York, 2021) pp. 171–180.
[34] T. B. Liverpool, Phys. Rev. E **101**, 042107 (2020).
[35] J. M. Raser and E. K. O'Shea, Science **309**, 2010 (2005).
[36] W. Razzell, W. Wood, and P. Martin, Dis. Models Mech. **4**, 569 (2011).
[37] H. Weavers, A. Franz, W. Wood, and P. Martin, JoVE **136**, e57871 (2018).
[38] See Supplemental Material at http://link.aps.org/supplemental/10.1103/PhysRevE.107.014403 for more details of experimental procedures and theoretical analyses.
[39] C. T. Rueden, J. Schindelin, M. C. Hiner, B. E. DeZonia, A. E. Walter, E. T. Arena, and K. W. Eliceiri, BMC Bioinf. **18**, 529 (2017).
[40] J. Schindelin, I. Arganda-Carreras, E. Frise, V. Kaynig, M. Longair, T. Pietzsch, S. Preibisch, C. Rueden, S. Saalfeld, B. Schmid *et al.*, Nat. Methods **9**, 676 (2012).
[41] S. Cross, Sjcross/modularimageanalysis: Version 0.7.21, (2018), DOI:10.5281/zenodo.2525263.
[42] M. Umorin, Stack focuser plugin for imagej, https://imagej.nih.gov/ij/plugins/stack-focuser.html (2002).
[43] L. Thuma, D. Carter, H. Weavers, and P. Martin, J. Cell Biol. **217**, 3045 (2018).
[44] I. Arganda-Carreras, V. Kaynig, C. Rueden, K. W. Eliceiri, J. Schindelin, A. Cardona, and H. S. Seung, Bioinformatics **33**, 2424 (2017).
[45] C. Steger, *IEEE Transactions on Pattern Analysis and Machine Intelligence* (IEEE, 1998), Vol. 20, pp. 113–125.

[46] F. Graner, B. Dollet, C. Raufaste, and P. Marmottant, Eur. Phys. J. E **25**, 349 (2008).
[47] P. Marmottant, C. Raufaste, and F. Graner, Eur. Phys. J. E **25**, 371 (2008).
[48] M. Esposito, Phys. Rev. E **85**, 041125 (2012).
[49] R. Zwanzig, J. Chem. Phys. **33**, 1338 (1960).
[50] M. Voliotis, N. Cohen, C. Molina-París, and T. B. Liverpool, Phys. Rev. Lett. **102**, 258101 (2009).
[51] A. Mogilner and E. Craig, J. Cell Sci. **123**, 3435 (2010).
[52] P. Sartori and S. Pigolotti, Phys. Rev. Lett. **110**, 188101 (2013).